

Monte Carlo Simulations of Shear-thinning Flow in Geological Fractures

Alessandro Lenci, Yves Méheust, M. Putti, V. Di Federico

▶ **To cite this version:**

Alessandro Lenci, Yves Méheust, M. Putti, V. Di Federico. Monte Carlo Simulations of Shear-thinning Flow in Geological Fractures. Water Resources Research, 2022, 58 (9), pp.e2022WR032024. 10.1029/2022wr032024 . insu-03760349v2

HAL Id: insu-03760349

https://insu.hal.science/insu-03760349v2

Submitted on 14 Sep 2022

HAL is a multi-disciplinary open access archive for the deposit and dissemination of scientific research documents, whether they are published or not. The documents may come from teaching and research institutions in France or abroad, or from public or private research centers.

L'archive ouverte pluridisciplinaire **HAL**, est destinée au dépôt et à la diffusion de documents scientifiques de niveau recherche, publiés ou non, émanant des établissements d'enseignement et de recherche français ou étrangers, des laboratoires publics ou privés.

Check for updates

Water Resources Research

RESEARCH ARTICLE
10.1029/2022WR032024

Monte Carlo Simulations of Shear-Thinning Flow in Geological Fractures

A. Lenci[1,2], Y. Méheust[2], M. Putti[3], and V. Di Federico[1]

[1]Department of Civil, Chemical, Environmental and Materials Engineering, Alma Mater Studiorum Università di Bologna, Bologna, Italy, [2]Géosciences Rennes, University Rennes, CNRS, Rennes, France, [3]Department of Mathematics, Università di Padova, Padua, Italy

Key Points:

- Monte Carlo simulations were conducted to investigate non-Newtonian hydrodynamics in rough fractures
- Shear-thinning behavior induces wider tails in the local flux PDF, emphasizes extreme flux values, and favors flow localization
- Shear-thinning behavior enhances the fracture's apparent transmissivity with respect to the Newtonian case

Correspondence to:
A. Lenci,
alessandro.lenci@unibo.it

Citation:
Lenci, A., Méheust, Y., Putti, M., & Di Federico, V. (2022). Monte Carlo simulations of shear-thinning flow in geological fractures. *Water Resources Research*, *58*, e2022WR032024. https://doi.org/10.1029/2022WR032024

Received 22 FEB 2022
Accepted 17 AUG 2022

© 2022. The Authors.
This is an open access article under the terms of the Creative Commons Attribution License, which permits use, distribution and reproduction in any medium, provided the original work is properly cited.

Abstract The hydraulic behavior of fractured rocks under shear-thinning flow is a challenging topic of interest in several fields, related either to environmental remediation or to natural resources recovery. The compound effect of fluid rheology and medium heterogeneity strongly affects flow and transport in fractured geological formations. Here, a stochastic analysis is conducted via Monte Carlo simulations to investigate the flow of shear-thinning fluids in fractures subjected to both natural and forced flow, considering different fracture dimensions, for a spatial correlation of the fracture that is an intrinsic parameter of the geological formation, independent of the fracture size. Considering the lubrication approximation, a generalized Reynolds equation for shear-thinning fluids is solved using an ad hoc, finite volume-based, numerical scheme. The influence of the rheology and aperture field heterogeneity on ensemble statistics of the velocity components and magnitude, as well as apparent fracture-scale transmissivity, is quantified over 10^3 fracture realizations. The probability density functions (PDFs) and relative confidence intervals, obtained by averaging over the statistics, are analyzed to characterize the apparent transmissivity transition from Newtonian to shear-thinning regime. The autocorrelation functions of velocity components are computed to understand the impact of rheology on spatial correlations the flow. Velocity components exhibit narrow PDFs with nearly exponential decay. More elevated pressure gradients emphasize the shear-thinning behavior, inducing a more pronounced flow localization, under otherwise identical conditions. This translates at the scale of the fracture into a larger apparent transmissivity as compared to the same configuration with Newtonian rheology, by orders of magnitude.

1. Introduction

Flow modeling of complex fluids in geological formations is of interest in numerous industrial applications. Among them are enhanced oil recovery (Hirasaki et al., 2011; Leung et al., 2014), geothermal circulations in fractured reservoirs (Bächler et al., 2003; Magzoub et al., 2021) and fluid losses during drilling operations (Feng & Gray, 2017), where foams, muds, emulsions, colloidal or non-colloidal suspensions are commonly involved. The use of high-viscosity gels in hydraulic fracturing improves the proppant carrying capacity and favors the generation of wider fractures in comparison to the use of slick water (Pahari et al., 2021). Drilling muds provide cooling and lubrication to the drill bit and are employed as mechanical stabilizers in the construction of the wellbore to pressurize the borehole against collapse. The constitutive law of these fluids does not respect Newton's law of viscosity, because their micro-structure induces a shear-thinning (ST) rheology at the continuum scale (Ansari et al., 2021; Barati & Liang, 2014). The non-Newtonian behavior of these fluids lies in their physical make-up and the ability of mesoscopic components to cross-link chemically (e.g., polymer solutions, see (Wang et al., 2016)) or interact electrostatically (e.g., colloidal suspensions, see Méheust et al., 2011; Parmar et al., 2008).

Subsurface geological formations (e.g., crustal rocks) are discontinuous media, consisting in matrix blocks of low permeability separated by fractures, which provide major conduits for flow. The connectivity among fractures and their hydraulic behavior are the features that control the entire formation permeability (Berkowitz, 1994). The simplest model to study the hydraulic behavior of a fracture is the parallel plate model or cubic law. This model has been largely used for its simplicity, although it oversimplifies wall topography. Different approaches have been proposed also to represent rough fractures: deterministic saw tooth (Wilson & Witherspoon, 1974), sinusoidal profiles (Elsworth & Goodman, 1986), or profiles with an assigned aperture probability distribution (Felisa et al., 2018; Lenci & Di Federico, 2020; Neuzil & Tracy, 1981). In minerals and rocks, however, field and laboratory measurements on fracture walls highlight the stochastic self-affine nature of the surface

morphology, for both natural (Brown & Scholz, 1985; Cox & Wang, 1993; Schmittbuhl et al., 1993) and fresh artificial fractures (Bouchaud, 1997; Schmittbuhl et al., 1993). Several algorithms are able to reproduce this kind of rough surfaces, which are more consistent with the experimental evidence: diamond-square algorithm (Fournier et al., 1982), successive random addition (Lu et al., 2003), and the FFT-based algorithm proposed by Méheust and Schmittbuhl (2003), which is far quicker.

Predictions of fracture transmissivities based on the parallel plate model significantly deviate from measurements, especially under elevated normal (Gale, 1990) or cyclic shear stresses (Makurat, 1985), limiting its use to sufficiently smooth fractures. Traditional computational fluid dynamics (Starchenko et al., 2016), lattice gas (Gutfraind et al., 1995; Stockman, 1997) and lattice Boltzmann methods (Meakin & Tartakovsky, 2009; Tian & Wang, 2017) have been adopted to capture the impact of the complex geometry of fractures on Newtonian flow, and thus to accurately predict flow and transport attributes, although the simulations are computationally intensive. Alternative numerical methods, based on lubrication theory and computationally more convenient, have been proposed to solve Newtonian creeping flow in rough fractures: standard matrix inversion techniques (Brown, 1987) or pseudospectral methods (Plouraboué et al., 1998). Estimation of the mean hydraulic aperture of a large number of independent fractures show a difference no larger than 2% (Mourzenko et al., 1995) between a lubrication-based solver and CFD simulations. Furthermore, due to the stochastic nature of the geometry of geological fractures, fractures described by the same statistical geometrical parameters can display a wide range of hydraulic behaviors (Méheust & Schmittbuhl, 2001, 2003), including cases that are more permeable than the parallel plate of identical mean aperture (Méheust & Schmittbuhl, 2000): thus the typical hydraulic behavior of a geological fracture should be understood as the average over a representative statistics, and the dispersion of the behaviors among the statistics should also be investigated. To our knowledge, Méheust and Schmittbuhl (2001) performed the first such Monte Carlo simulations of Newtonian creeping flow in geological fractures with realistic geometries.

Monte Carlo simulations have been adopted for decades to simulate different processes in a variety of geologic media: a limited number of realizations of 1-D fractures with variable aperture were produced by Tsang and Tsang (1987) to investigate flow in fracture channels; the same approach was then generalized to 2-D fractures, although with spatial distributions of apertures that are more relevant to 2-D aquifer permeability fields than to geological fractures (Moreno et al., 1988). The pioneering work of Bellin et al. (1992) investigated the conditions for the validity of first-order flow and transport theories in random porous media; Berkowitz and Scher (1998) adopted a Monte Carlo approach to determine velocity distributions in fracture networks, as a function of the fracture orientations, to study anomalous transport at the network scale; Gómez-Hernández and Wen (1998) analyzed the applicability of multi-Gaussian random function models in hydrogeology. More recently this methodology has been applied to study transient sequentially coupled radionuclide transport (Hayek et al., 2020), to investigate flow in two dimensional (2-D) conductivity fields and derive a large-scale transport model (Comolli et al., 2019), to simulate CO_2 plume migration (Zhong et al., 2019), and to perform uncertainty quantification (Yang et al., 2020).

Notwithstanding the ubiquitous use of complex fluids in the subsurface, their rheology is often taken to be Newtonian, with a limited number of studies having focused on non-Newtonian flow. Several analytical expressions have been proposed to comprehend the flow features in simple geometries (Larson, 1992), or to qualitatively assess the effect of fluid rheology on flow in a variable aperture field of given distribution (Di Federico, 1997). Different numerical strategies have been adopted to handle non-linear problems when dealing with a complex rheology in a variable aperture field: Picard's method (Morris et al., 2015), and sequential sweeping (Lavrov, 2013). A few studies have also addressed non-Newtonian flow in fractures with self-affine geometries (Auradou et al., 2008; Lenci et al., 2022; Perkowska et al., 2016). Recently, advances in computational power have allowed the investigation of complex processes, such as: multiphase flow (Katiyar et al., 2020), transport in fractures of permeable walls (Dejam, 2019), and hydro-mechanical coupling (Chiapponi et al., 2019; Ciriello et al., 2021; Moukhtari & Lecampion, 2018; Wrobel et al., 2021).

Despite this wealth of contributions using different constitutive models and hypotheses, to date stochastic analyses have never been applied to investigate ST hydrodynamics in rough fractures under natural and artificial flow conditions. In this study we extend the state of the art by exploring the non-Newtonian, ST, hydraulic behavior of a rough fracture within a stochastic framework, using a depth-integrated, 2-D, flow model proposed by Lenci et al. (2022). A total of twelve thousand Monte Carlo simulations are run, with fractures partitioned adopting a

million node regular mesh. A stochastic analysis of this phenomenon has never been conducted due to the limitations of numerical tools available prior to Lenci et al. (2022). Existing studies in the literature typically involve one or few realizations and adopt small meshes (e.g., 33×33 in Lavrov (2013)) to achieve convergence in a reasonable amount of time. Here, we conduct a systematic analysis of the main quantities of interest in a variable aperture fracture, the velocity field and the transmissivity, by exploring their probabilistic behavior. We do so in dimensionless form, starting from realistic values of dimensional parameters typical of the aforementioned subsurface applications. We thus unravel the intertwined roles of ST rheology and fracture heterogeneity.

The article is organized as follows: Section 2 presents the non-linear lubrication equation for a non-Newtonian Ellis fluid, the generation process of discrete fractures, and describes the implementation of the lubrication-based numerical code; in Section 3, the adopted stochastic approach is outlined; Section 4 presents the results of the Monte Carlo simulations performed, emphasizing the ensemble statistics obtained: these include the apparent transmissivity, the vertical and longitudinal velocity components, and the velocity modulus; the covariance of the latter is also analyzed. Conclusions and perspectives for future work are formulated in Section 5.

2. Modeling Framework

2.1. Generation of Synthetic Fractures

A geological fracture is composed of two rough walls, whose parallel mean planes are separated by $\langle w \rangle$, defined as the mechanical aperture. The topographies of the upper (z_u) and lower wall (z_l), assumed of zero mean, fluctuate with respect to their mean planes, and local apertures can be defined as the distance between them; at positions where the two walls interpenetrate, a zero aperture is imposed:

$$w(x, y) = \max\left(0, z_u(x, y) - z_l(x, y) + \langle w \rangle\right) \quad . \tag{1}$$

Fracture surfaces exhibit long-range spatial correlation (Candela et al., 2009; Schmittbuhl, Vilotte, & Roux, 1995). Therefore, the topography of a geological fracture's rough wall is an isotropic self-affine surface, with the probability densit function (PDF) $f(\Delta z, \Delta r)$ scaling as:

$$\forall \lambda, \qquad f(\Delta z, \Delta r) = \lambda^H f\left(\lambda^H \Delta z, \Delta r\right), \tag{2}$$

where Δz is the height difference between two points separated by an in-plane segment of length Δr, H is the Hurst exponent, and λ is a scaling factor. Note that fracture surfaces in crystalline rocks consistently show a Hurst exponent of 0.8 (Méheust & Schmittbuhl, 2000), and this value has been proposed as universal by Bouchaud et al. (1990). However, exceptions exist, such as sandstones, in which the grain-induced roughness regime, for high frequencies in the power spectrum, may present values close to 0.5 (Boffa et al., 1999; Nigon et al., 2017). One consequence of the scaling property of the PDF in Equation 2 is that the 2-D power density spectrum of wall topography scales as a power law of the wave number in the form $S(k) \propto k^{-2(1+H)}$, where the wave number k is the norm of the wave vector, that is, $k = \left(k_x^2 + k_y^2\right)^{1/2}$, k_x and k_y being the components of the wave vector.

The two walls of a geological fracture are matched at large length scales (i.e., their large scale topographies are identical), but differ at scales smaller than a crossover scale, which we shall denote the correlation length L_c (Brown, 1995). This is due to mechanical wear and chemical weathering over long times. It follows that the aperture field exhibits the same self-affinity as the walls at scales smaller than L_c, and, thus, that the aperture field's Fourier spectrum exhibits the characteristic self-affine power-law scaling at these small scales, and an almost flat behavior due to the matching of the two walls at scales larger than L_c. Consequently, the spectral power density of the aperture field exhibits the above-mentioned power-law radial decay, of negative exponent $-2(H + 1)$ for wave numbers higher than k_c, the characteristic wave number corresponding to scale L_c (Schmittbuhl, Schmitt, & Scholz, 1995), and is flat for wave numbers smaller than k_c.

This property can be used to generate realistic synthetic aperture fields from a 2-D white noise, maintaining its random phase and introducing the spatial correlations by multiplying the Fourier modes corresponding to scales smaller than L_c by the power-law behavior $k^{-(H+1)}$ (Méheust & Schmittbuhl, 2003). Applying an inverse Fourier transform then yields an aperture field with the appropriate geometry, which can then be scaled and translated vertically so as to impose the desired mean aperture and standard deviation of aperture fluctuations. Figure 1a depicts the 2-D Fourier spectrum of such a synthetic aperture field, while Figure 1b presents its aver-

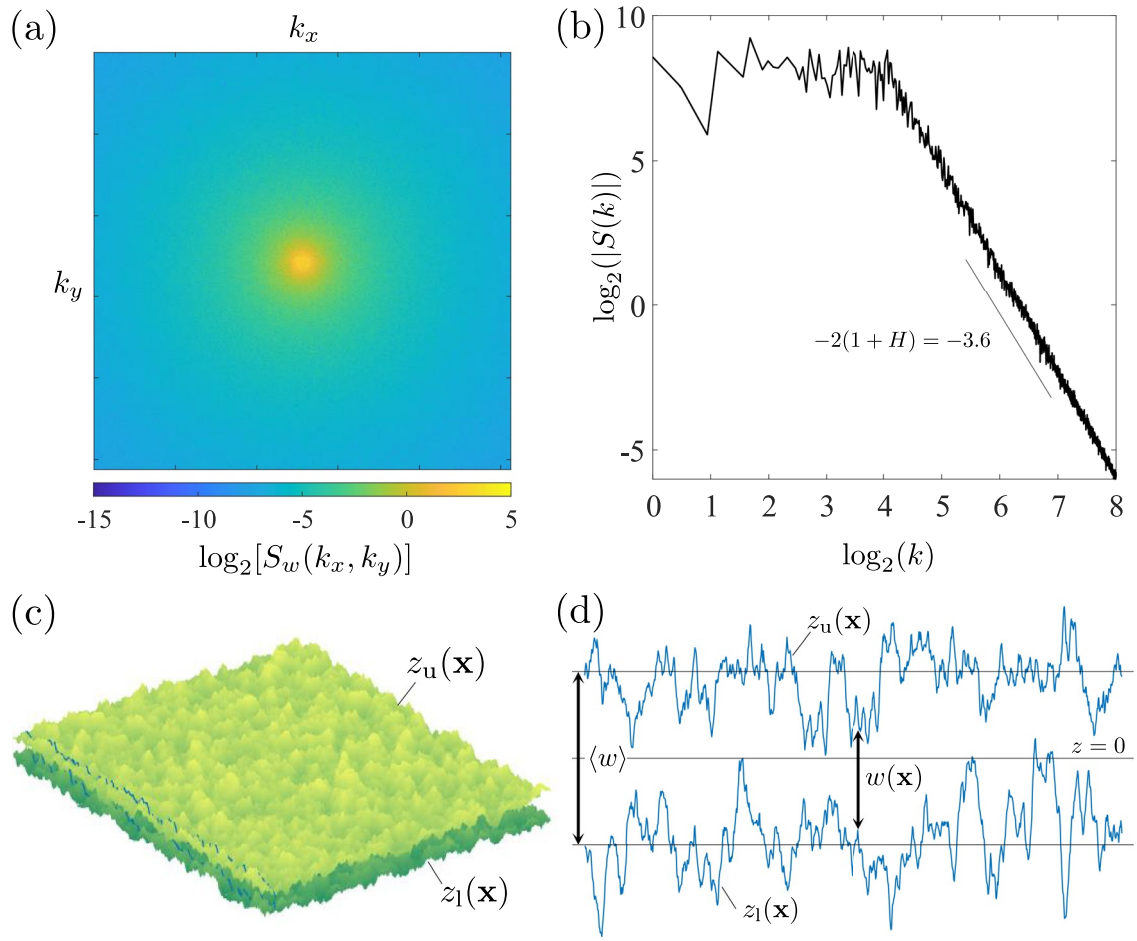


Figure 1. (a) Binary logarithm of the power density spectrum of a synthetic fracture's aperture field, plotted as a function of the Fourier modes k_x and k_y (in linear scale); the isotropic spectrum is stochastic and exhibits the typical radial power law decay $\propto \left(k_x^2 + k_y^2\right)^{-(1+H)}$ for wave numbers $k = \sqrt{k_x^2 + k_y^2}$ larger than k_c, and is constant otherwise ($k \leq k_c$). (b) Radial profile obtained by averaging the spectrum in (a) over the azimuthal angles; it shows the aforementioned self-affine behavior more clearly. (c) 3-D representation of the fracture's rough walls. (d) 2-D cross-section of the fracture, corresponding to the blue lines in (c), with geometrical quantities of interest. The vertical scale is 10 times larger than the horizontal scale. Other adopted parameters are: the Hurst exponent $H = 0.8$, mean aperture $\langle w \rangle = 10^{-3}$ m, correlation length, $L_c = 0.1$ m, closure $\sigma_w/\langle w \rangle = 0.3$ and correlation ratio $L/L_c = 16$, with L fracture size.

age radial profile, with the scaling properties discussed above. Figure 2 shows the comparison between two different aperture fields having the same correlation length but different fracture sizes, and thus a markedly different size-to-correlation-length ratio. The latter parameter will be later seen to affect the flow behavior quite significantly.

2.2. Flow Model

2.2.1. Generalized Reynolds Equation

We consider the steady-state, isothermal Stokes flow of an incompressible fluid between two smooth parallel straight walls separated by a uniform distance w. Under the lubrication approximation (Brown, 1987), if the aperture field remains sufficiently smooth ($\nabla w \ll 1$), the vertical component of the velocity is negligible with respect to the horizontal component. Consequently, the pressure field is independent of the coordinate z whose axis is perpendicular to the mean fracture plane, and the projection of the momentum balance on that plane can be written as

$$\frac{\partial}{\partial z}\left(\mu \frac{\partial \mathbf{u}}{\partial z}\right) = \boldsymbol{\nabla}_{\parallel} P, \tag{3}$$

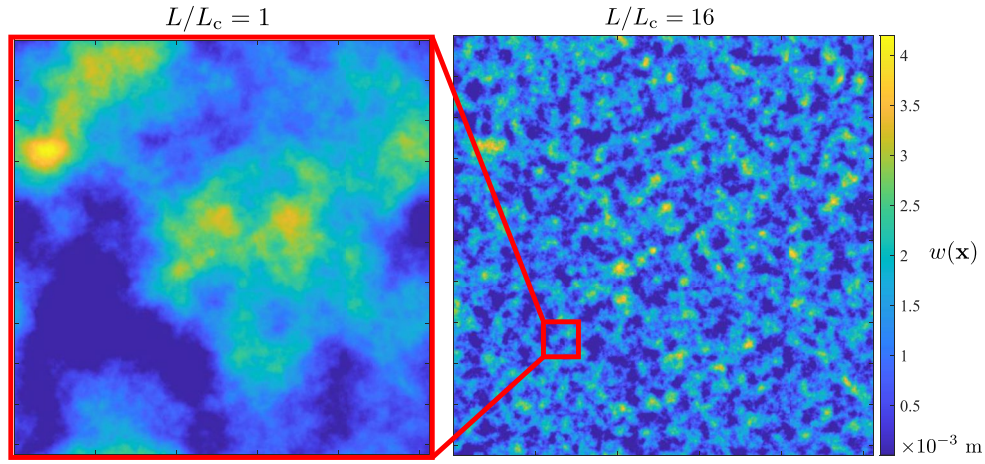


Figure 2. Comparison between aperture fields for different values of L/L_c, with L fracture size; the color bar reports the aperture magnitude in meters for both representations. The two realizations are generated with a Hurst exponent $H = 0.8$, a closure $\sigma_w/\langle w\rangle = 0.8$, a correlation length $L_c = 10^{-1}$ m, and a mean aperture $\langle w\rangle = 10^{-3}$ m. The red frames illustrate the size ratio between the two fractures, which is 16.

where $\mathbf{u}$ is the velocity vector, $\nabla_{\parallel}P$ is the projection of the pressure gradient onto the fracture plane, and μ is the dynamic viscosity or the apparent viscosity if the fluid is Newtonian or non-Newtonian, respectively. After defining the mean value $\bar{z}(x, y)$, which indicates the middle point of the fracture at position (x, y) along the fracture plane, and integrating once over the z-direction between $\bar{z}(x, y)$ and z, the momentum conservation becomes (Lenci et al., 2022)

$$\mu \frac{\partial \mathbf{u}}{\partial z} = (z - \bar{z})\, \boldsymbol{\nabla}_{\parallel} P, \tag{4}$$

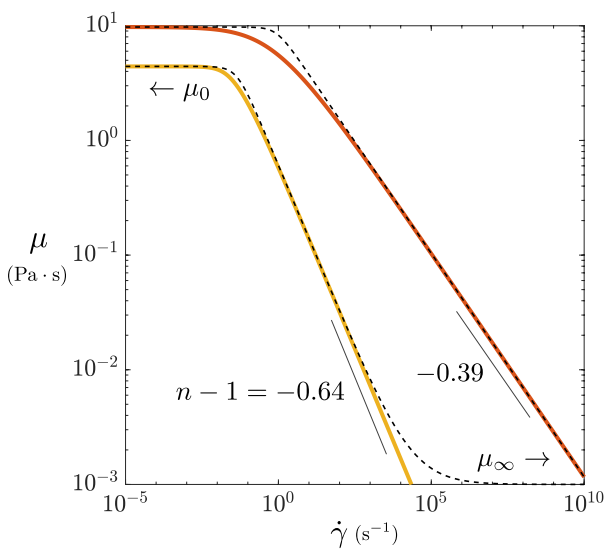


Figure 3. Dependence of the apparent viscosity μ on the shear rate $\dot{\gamma}$. The constitutive equation is represented for two Ellis fluids of different ST behavior: a xanthan gum, the yellow-solid line, and a silicon oil, the orange-solid solid lines. Both fluids show a low-shear rate Newtonian plateau ($\mu \rightarrow \mu_0$), while black-dashed lines represent the original Carreau model. The black dashed lines are similar curves obtained for two Carreau fluids with the same low-shear plateaus and power law behaviors as each of the two Ellis fluids, respectively, and a high shear asymptotic viscosity of 10^{-3} Pa ·s, similar to water's, for one of them (the other one's high shear plateau is not visible).

where we notice that the left term is actually the definition of the shear stress $\boldsymbol{\tau}$. The projection of the momentum balance onto the z axis shows that the component of ∇P along that axis can be neglected, so in the following we replace the notation $\nabla_{\parallel}P$ above by ∇P.

For a generalized Newtonian model, the apparent viscosity can be expressed in terms of the shear stress or shear rate. In particular, the Ellis fluid rheology is a three-parameter model in which the apparent viscosity is related to the magnitude τ of $\boldsymbol{\tau}$ according to

$$\mu = \mu_0 \left[1 + \left(\frac{\tau}{\tau_{1/2}}\right)^{\frac{1}{n}-1}\right]^{-1}, \tag{5}$$

where μ_0 is the dynamic viscosity at low shear rates, n is the ST index that defines the power-law trend at high-shear stress, and $\tau_{1/2}$ is a characteristic shear stress such that $\mu(\tau_{1/2}) = \mu_0/2$. This model reduces to a Newtonian rheology either for $n = 1$ or $\tau_{1/2} \rightarrow \infty$. For $n = 1$ the fluid presents a constant dynamic viscosity $\mu = \mu_0/2$, whereas for $\tau_{1/2} \rightarrow \infty$ and $n < 1$ the transition from Newtonian plateau to the power law trend occurs at infinite shear stress (or equivalently, shear rate), which yields a constant viscosity $\mu = \mu_0$. In Figure 3, the dependence of the apparent viscosity on the shear rate is represented in colors for two examples of Ellis fluids, showing the low shear-rate quasi-Newtonian plateau and the high shear rate ST power-law trend.

The local flux $\boldsymbol{q}$ is defined as the integral of the 3-D fluid velocities over the local fracture aperture $w(x)$ (i.e., along the direction transverse to the mean fracture plane) (Méheust & Schmittbuhl, 2001). If the fluid is Newtonian, the

relationship between $\boldsymbol{q}$ and the local pressure gradient ∇P is given by the Hagen-Poiseuille law, which effectively expresses Darcy's law with an intrinsic permeability $w^2/12$. Similarly, for the Ellis model it is possible to analytically derive the velocity profile by introducing the expression of τ as a function of ∇P (from Equation 4) in Equation 5, and integrating between the value of z at the lower wall (at which the velocity is zero) and z. We thus obtain

$$\mathbf{u}(z) = -\left\{ \frac{1}{8\mu_0}\left[w^2 - 4z^2\right] + \frac{n}{n+1}\left(\frac{1}{2^{n+1}\mu_0^n \tau_{1/2}^{1-n}}\right)^{\frac{1}{n}} \left[w^{\frac{1}{n}+1} - 2^{\frac{1}{n}+1}|z|^{\frac{1}{n}+1}\right] ||\nabla P||^{\frac{1}{n}-1} \right\} \nabla P. \tag{6}$$

For $n = 1$ (or $\tau_{1/2} \to 0$), Equation 6 returns the Newtonian, parabolic, velocity profile and leads to the aforementioned Hagen-Poiseuille law after integration over the fracture's cross section. In general case, this integration leads to a generalized, non-linear relation between the local flux and the pressure gradient:

$$\mathbf{q} = -\left[\frac{w^3}{12\mu_0} + \frac{n}{2n+1}\left(\frac{1}{2^{1+n}\mu_0^n \tau_{1/2}{}^{1-n}}\right)^{\frac{1}{n}} w^{\frac{2n+1}{n}} \|\nabla P\|^{\frac{1}{n}-1} \right] \nabla P \ . \tag{7}$$

It follows from the definition of $\mathbf{q}$, from the mass conservation for the incompressible fluid (continuity equation, $\nabla \cdot \mathbf{u} = 0$), and from the nullity of fluid velocities at the fracture's walls, that $\mathbf{q}$ is conservative ($\nabla \cdot \mathbf{q} = 0$). Introducing Equation 7 in the conservation of $\mathbf{q}$ yields the generalized Reynolds equation:

$$-\boldsymbol{\nabla} \cdot \left[\left(\frac{w^3}{12\mu_0} + \frac{n}{(2n+1)}\left(\frac{1}{2^{1+n}\mu_0^n \tau_{1/2}^{1-n}}\right)^{\frac{1}{n}} w^{\frac{2n+1}{n}} \|\nabla P\|^{\frac{1}{n}-1} \right) \nabla P \right] = 0, \tag{8}$$

which for $n = 1$ (Newtonian fluid) reduces to the classical Reynolds equation (Brown, 1987).

The mean flow velocity at position (x, y) (i.e., vertically-averaged local velocity) is then defined as:

$$\overline{\mathbf{u}} = \frac{\mathbf{q}}{w} = -\left[\frac{w^2}{12\mu_0} + \frac{n}{2n+1}\left(\frac{1}{2^{1+n}\mu_0^n \tau_{1/2}{}^{1-n}}\right)^{\frac{1}{n}} w)^{\frac{n+1}{n}} \|\nabla P\|^{\frac{1}{n}-1} \right] \nabla P \ . \tag{9}$$

Hereinafter, the magnitudes of the velocity $\overline{\mathbf{u}}$ and of its longitudinal and transversal components, $\overline{\mathbf{u}}_x$ and $\overline{\mathbf{u}}_y$, are denoted $\overline{u}$, $\overline{u}_x$ and $\overline{u}_y$, respectively.

2.2.2. From Fitted Carreau Model Parameters to Ellis Model Parameters

In the literature, the four-parameter Carreau model (Carreau, 1972) is commonly adopted to fit rheological data for ST fluids, with the apparent viscosity expressed as a function of the shear rate as follows:

$$\mu = \mu'_\infty + \frac{\mu'_0 - \mu'_\infty}{\left[1 + \left(\frac{\dot{\gamma}}{\dot{\gamma}_c}\right)^2\right]^{\frac{1-n'}{2}}} \ . \tag{10}$$

This model features a high viscosity $\left(\mu \simeq \mu'_0\right)$ plateau and a low viscosity $(\mu \simeq \mu'_\infty)$ plateau at low and high shear rates, respectively. These plateaus are separated by a power law ST trend of exponent, or ST index, n' (see black dashed lines in Figure 3)); $\dot{\gamma}_c$ is a characteristic shear rate that regulates the transition from the low-shear rate viscosity plateau to the ST behavior.

Such plateaus are observed on experimental rheology data for ST fluids, which is why the Carreau model is well indicated. However, the Carreau constitutive equation does not allow deriving an explicit analytical expression of the flow rate as a function of the imposed pressure gradient. Alternatively, the Ellis model exhibits a high-viscosity low-shear rate plateau as well, but lacks the high-shear rate low-viscosity additional plateau, typical of the Carreau model. Due to the modest influence on the flow of the latter low-viscosity plateau, except at exceptionally high imposed macroscopic pressure gradient, the Ellis model represents a valid alternative to the Carreau model to simulate creeping flow of a ST fluid in variable aperture fractures. In this work, parameters for the Ellis model are inferred from the Carreau parameters fitted to experimental data of real fluids by Uddin

et al. (2012). These parameters are obtained assuming the same low-shear rate viscosity plateau $\left(\mu_0 = \mu_0'\right)$, and the same ST behavior at moderate to large shear rates. The latter conditions imposes both $n = n'$ and the value for the characteristic shear stress $\tau_{1/2}$. In particular, for $\dot{\gamma} \gg \dot{\gamma}_c$, the Carreau model can be re-written as

$$\mu \underset{\dot{\gamma} \gg \dot{\gamma}_c}{\sim} \mu_0' \left(\frac{\dot{\gamma}_c}{\dot{\gamma}} \right)^{1-n'}, \tag{11}$$

while similarly, for $\tau \gg \tau_{1/2}$, the Ellis model becomes

$$\mu \underset{\tau \gg \tau_c}{\sim} \mu_0 \left(\frac{\tau_{1/2}}{\tau} \right)^{\frac{1-n}{n}} = \mu_0 \left(\frac{\tau_{1/2}}{\mu \dot{\gamma}} \right)^{\frac{1-n}{n}}. \tag{12}$$

Equations 11 and 12 thus provide a simple expression of $\tau_{1/2}$ in terms of the Carreau parameters:

$$\tau_{1/2} = \mu_0 \dot{\gamma}_c \ . \tag{13}$$

2.2.3. When to Expect a Shear-Thinning Behavior?

From now on we shall denote $\overline{\nabla P}$ the macroscopic pressure gradient, that is, the pressure gradient that is imposed at the fracture scale. The behavior of the fluid inside the fracture will be all the more ST as $\overline{\nabla P}$ is larger. A critical macroscopic pressure gradient $\overline{\nabla P}_c$, above which the non-linear rheology starts to manifest itself in the flow, can be analytically derived in the following manner. Considering the parallel plate configuration of aperture equal to the rough fracture's mean aperture, when the maximum shear rate occurring in the flow (τ_{max}) is higher than the critical shear rate $\tau_c = \tau(\dot{\gamma}_c)$, the viscosity starts to deviate from the Newtonian plateau viscosity μ_0. Given Equation 4, the critical pressure gradient can be estimated as

$$\overline{\boldsymbol{\nabla} P_c} = \frac{2\tau_c}{\langle w \rangle}, \tag{14}$$

where the critical shear stress τ_c can be numerically evaluated from

$$\tau_c = \mu_0 \left[1 + \left(\frac{\tau_c}{\tau_{1/2}} \right)^{\frac{1}{n}-1} \right]^{-1} \dot{\gamma}_c \ . \tag{15}$$

Moreover, following Zami-Pierre et al. (2016) (who were addressing ST flow in porous media), we define the characteristic local flow rate magnitude q_c for which transition from Newtonian to ST is expected to occur, as:

$$q_c = \dot{\gamma}_c \langle w \rangle \sqrt{k_0}, \tag{16}$$

where k_0 is the fracture intrinsic permeability defined classically for Newtonian flow.

2.3. Flow Solver

A lubrication-based numerical code has been implemented to solve Equation 8 in a single fracture (Lenci et al., 2022), whose aperture geometry is generated by means of the synthetic fracture generator described in Section 2.1. A fracture of dimensions $L \times L$ along its mean plane is discretized on a $N \times N$ regular grid, the flow resulting from an imposed pressure drop $P_0 - P_1$ between the inlet (left-hand boundary) and outlet (right-hand boundary) of the fracture, along the x-direction. The corresponding macroscopic pressure gradient is $\overline{\nabla P} = (P_0 - P_1)/L$. No-flow conditions are imposed along the two transverse boundaries of the flow domain.

A finite volume scheme has been adopted to solve the flow (see Figure 4). The pressure $P(x, y)$ and aperture $w(x, y)$ are defined at different locations, on a staggered grid. The pressure is defined at the center of each mesh cell, the aperture on the boundary between neighboring cells via arithmetic mean (e.g., $w_i^{(j)} = (w_j + w_i)/2$). The discrete formulation of Equation 8 can be written for node j as

$$\sum_{i \in \sigma(j)} \left[\frac{{w_i^{(j)}}^3}{12\mu_0} + \frac{n}{2n+1} \left(\frac{1}{2^{n+1} \mu_0^n \tau_{1/2}^{1-n}} \right)^{\frac{1}{n}} {w_i^{(j)}}^{\frac{2n+1}{n}} \left| \frac{P_i - P_j}{\Delta} \right|^{\frac{1}{n}-1} \right] \left(\frac{P_i - P_j}{\Delta} \right) = 0, \tag{17}$$

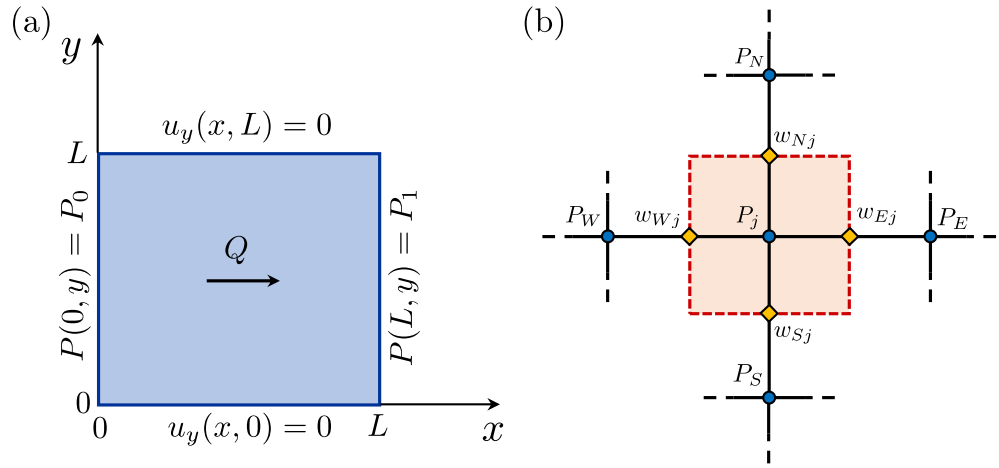


Figure 4. (a) Fracture representation with boundary conditions and flow rate direction. (b) Finite volume five-point stencil: the pressure is defined at the center of the finite volumes (indicated by the blue nodes), the aperture at the center of the edges (indicated by the yellow nodes) via arithmetic mean.

where $\sigma(j) = \{N, S, E, W\}$ is the set of cells neighboring the jth cell, and $\Delta = L/N$ is the mesh size.

The resulting non-linear system of equations is solved with an inexact Newton-Krylov method, wherein the linearized symmetric system of equations is solved via variable-fill-in incomplete Cholesky preconditioned conjugate gradient (ICPCG) and a parameter continuation strategy is adopted for configurations with strong non-linearities (i.e., small values of the exponent n). The solver is described in detail in Lenci et al. (2022).

The numerical code is introduced in a parallel computing framework and outputs are saved and stored using a high-performance hierarchical data format (Koranne, 2010) to reduce the computational time required by the MC simulations and the post-processing.

3. Stochastic Analysis

3.1. Application Scenarios

In this study, we consider the Ellis model for two ST fluids which have been selected such that the power-law exponents n differ sensibly between them and the viscosity cut-offs μ_0 are similar, while no particular requirements are imposed to $\tau_{1/2}$. The Carreau parameters of a silicon oil fluid are taken from Uddin et al. (2012), while the other fluid is an ad hoc xanthan gum fluid produced in the laboratory. Table 1 lists the properties of these two non-Newtonian fluids, while Figure 3 depicts the corresponding constitutive laws in an apparent viscosity versus shear rate plot. In the following, the flow of the two ST fluids will be compared to that of a Newtonian fluid of dynamic viscosity equal to μ_0.

The analysis is conducted for different imposed macroscopic pressure gradients $\overline{\nabla P}$ and fracture lengths L. The former ranges from 10^2 to 10^3 Pa/m, which corresponds to typical orders of magnitude of groundwater natural potential gradients (Zimmerman & Bodvarsson, 1996), to 10^4 Pa/m, which can be associated with artificially-induced flow in hydraulic fracturing operations (Jung, 1989). Assuming a constant correlation length $L_c = 0.1$ m, a fracture length $L = 0.1$ m and a larger one $L = 1.6$ m are considered to illustrate the impact of the L/L_c ratio on the flow. Indeed, if one considers that the correlation length is a property of the formation, resulting from tectonic constrains and chemical weathering posterior to fracturing, then we can assume it to be independent of the fracture's length (de Dreuzy et al., 2012); hence L/L_c increases as the fracture length increases. Regarding the mean aperture, in situ measurements of fracture apertures are challenging (Barbati et al., 2016), thus mean apertures are typically obtained from rough wall measurements on laboratory samples. Typical values of mean fracture

Table 1
Rheologic Parameters for the Two Considered Fluids: A Silicon Oil (Uddin et al., 2012) and a Xanthan Gum Produced in the Laboratory

	Carreau Model				Ellis Model		
Fluid (ID)	n'	μ_0'	μ_∞'	$\dot{\gamma}_c$	n	μ_0	$\tau_{1/2}$
	(−)	(Pa s)	(Pa s)	(s^{-1})	(−)	(Pa s)	(Pa)
Silicon oil (SO)	0.61	9.75	0	0.045	0.61	9.75	8.48
Xanthan gum (XG)	0.36	4.42	10^{-3}	0.869	0.36	4.42	0.20

Experimental data are originally fitted with the Carreau model, after which Ellis parameters are inferred analytically from the fitted parameters.

Table 2
List of the Fracture Generator's Inputs That Are Common to All MC Simulations and Realizations

Correlation Length	L_c	(m)	10^{-1}
Mean Aperture	$\langle w \rangle$	(m)	10^{-3}
Aperture Coefficient of Variation	$\sigma_w/\langle w \rangle$	(−)	0.8
Hurst Exponent	H	(−)	0.8
Mesh size	$N \times N$	(−)	$2^{10} \times 2^{10}$

aperture range from 0.1 to 10 mm (Cipolla et al., 2008). However, values close to 1 mm are more frequent (Nowamooz et al., 2013; Yeo et al., 1998).

3.2. Monte Carlo Simulations

In total, twelve (12) Monte Carlo (MC) sets of simulations have been performed. For each MC set, NMC = 10^3 fracture realizations were generated, changing the seed of the Mersenne Twister random number generator (RNG) (Matsumoto & Nishimura, 1998); see the generation algorithm in Lenci et al. (2022). Table 3 reports the parameters μ_0, n and $\tau_{1/2}$ describing the fluid, the correlation length to length ratio, and the pressure gradient for all 12 MC sets, whereas the geometric parameters are listed in Table 2. The flow was then computed for each fracture realization of each MC set. The acceptance criterion is based on the exit tolerance of the Newton method and on the respect of the mass conservation over the fracture domain. When such requirements were not met, the number of parameter continuation steps (see Section 2.3) were increased until the criterion was fully satisfied. In fact, no simulations needed to be discarded in this analysis. The numerical code provides the following quantities of interest (QoI) for each process realization: the pressure field (P), the longitudinal velocity component $(\overline{u}_x)$, the transversal velocity component $(\overline{u}_y)$, the velocity magnitude, and the apparent transmissivity (T). For non-Newtonian flow in fractures, the apparent transmissivity can be defined as:

$$T = \frac{Q\mu_0}{\overline{\nabla P}}, \tag{18}$$

where Q is the volumetric flow rate. Note that for a ST rheology this transmissivity is not an intrinsic property of the fracture, and will depend on the mean velocity, or, equivalently, on the imposed macroscopic pressure gradient. As n goes to 1, T reduces to T_0, which does not depend on the velocity magnitude but only on the fracture's geometry, for a Newtonian fluid.

The post-processing phase elaborates the outputs and produces PDFs of the dimensionless QoIs for each realization; then, it computes the ensemble average of the PDFs with the relative confidence interval, estimated considering a range of one standard deviation around the mean. In the following section, results concerning the non-Newtonian hydraulic behavior of variable aperture fractures are discussed with a probabilistic approach; to this end, the velocity components ($\overline{u}_x$ and $\overline{u}_y$) are normalized by the mean velocity magnitude $(\langle \overline{u} \rangle)$, that is, the average over the fracture plane of the velocity $\overline{\mathbf{u}}$ (which is itself the fluid velocity averaged over the local aperture). More generally, in the following we shall denote by $\langle \cdot \rangle$ the spatial average of any quantity over the fracture plane.

4. Results

4.1. Probability Density Functions of Depth-Averaged Flow Velocities

A thorough analysis based on the Monte Carlo framework discussed in the previous section has been conducted to characterize the steady isothermal Stokes flow of ST fluids in rough fractures. Figure 5 provides an example of the spatial distribution of fluid velocities in the fracture plane of two fracture realizations with different values of the size-to-correlation-length ratio L/L_c. The velocity fields were obtained by solving the lubrication-based model described in Section 2. The flow is mainly cocurrent, but local backward flow (i.e., negative $\overline{u}_x/\langle \overline{u} \rangle$ values) may occur due to contrasting adjacent aperture values near the fracture contact zones; these, in turn, occupy a good percentage of the fracture total surface (about 30%) for the selected coefficient of variation of the aperture field, which is $\sigma_w/\langle w \rangle = 0.8$. Flow localization is all the stronger as the ST fluid index n is smaller; this effect has been studied in detail by Lenci et al. (2022).

The stochastic velocity dynamics is analyzed by means of the ensemble average PDFs of the longitudinal and transversal velocity components, and of the velocity magnitude. Moreover, the confidence interval is provided for each PDF to measure the dispersion of the results around the mean behavior.

The ensemble average PDFs of the longitudinal component of the velocity are depicted in Figure 6 for all parameter combinations listed in Table 3. The PDFs of the longitudinal velocity component are distinctly narrow, with

Table 3
ID-Numbers of the Monte Carlo Sets, and Related Parameters: Fluid Rheology (μ_0, $\tau_{1/2}$, n), Ratio of Fracture Size to Correlation Length L/L_c, Pressure Gradient $\overline{\nabla P}$, and Ratio of Pressure Gradient to Critical Pressure Gradient $\overline{\nabla P}/\overline{\nabla P_c}$

MC set	μ_0 (Pa · s)	$\tau_{1/2}$ (Pa)	n (−)	L/L_c (−)	$\overline{\nabla P}$ (Pa · m^{-1})	$\overline{\nabla P}/\overline{\nabla P_c}$ (−)
MC1	4.42	8.48	0.36	1	10^2	2.0×10^{-1}
MC2	4.42	8.48	0.36	1	10^3	2.2×10^{0}
MC3	4.42	8.48	0.36	1	10^4	2.2×10^{1}
MC4	4.42	8.48	0.36	16	10^2	2.0×10^{-1}
MC5	4.42	8.48	0.36	16	10^3	2.2×10^{0}
MC6	4.42	8.48	0.36	16	10^4	2.2×10^{1}
MC7	9.75	0.20	0.61	1	10^2	6.5×10^{-4}
MC8	9.75	0.20	0.61	1	10^3	6.5×10^{-3}
MC9	9.75	0.20	0.61	1	10^4	6.5×10^{-2}
MC10	9.75	0.20	0.61	16	10^2	6.5×10^{-4}
MC11	9.75	0.20	0.61	16	10^3	6.5×10^{-3}
MC12	9.75	0.20	0.61	16	10^4	6.5×10^{-2}

The ratio $\overline{\nabla P}/\overline{\nabla P_c}$ is reported to quantify the significance of non-linear effects. Other parameters common to all simulations are listed in Table 1.

the positive cocurrent part exhibiting a decay which approaches an exponential decay for $L/L_c = 16$, and a stretched exponential for $L/L_c = 1$. A similar behavior was observed in two and 3-D porous media flows, for Newtonian (Siena et al., 2014) and non-Newtonian fluids (Zami-Pierre et al., 2016), which is not surprising since the rough fractures behave all the more as a 2-D porous medium as the correlation length is smaller. Indeed, a smaller correlation length means that spatial correlations in the apertures (which is essentially what distinguishes a fracture geometry from an uncorrelated 2-D porous medium) are restricted to a narrower range of scales, at small scales. Under strongly forced flow conditions, that is, the highest values of the pressure gradient, the strongly shear thinning fluid ($n = 0.36$) exhibits wider cocurrent and thinner countercurrent tails with respect to the less shear thinning fluid ($n = 0.61$), and even more so when compared to the Newtonian case in the same conditions. On the other hand, under lower pressure gradients the PDFs for Newtonian and non-Newtonian fluids almost overlap, clearly indicating that the fracture heterogeneity governs the flow and the nonlinear effects associated to rheology are quite modest. Results for small fractures (i.e., $L/L_c = 1$) are almost independent of the rheology and flow regime, with a very modest increase/decrease of the cocurrent/countercurrent tail only for the most ST fluid and the highest pressure gradient. In this type of geometry the strong channeling resulting from the aperture field heterogeneity, which is correlated up to the fracture size, dominates over the effect of rheology. Although the ST flow is faster than Newtonian flow under identical conditions (see Lenci et al., 2022), the PDF of the longitudinal velocity component normalized by the average velocity is little impacted by the rheology. For large fractures ($L/L_c = 16$) the effect is reversed but remains extremely modest for the lowest considered value of $\overline{\nabla P}$.

Figure 7 depicts the ensemble average PDFs of the transversal velocity components: these are nearly symmetric around zero as expected. Results for small fractures (i.e., $L/L_c = 1$) are invariant with respect to the rheology and flow regime, with no significant differences for any combination of parameters. Again this behavior results from the strong geometry-mediated channeling. On the other hand, large fractures ($L/L_c = 16$) under high pressure gradient show wider tails, especially for the most shear thinning fluid. The PDFs of the transverse velocity components suggest, similarly to the longitudinal case, that under low pressure gradients the flow pattern is mainly dominated by fracture heterogeneity, with contributions due to non-linear rheology that arise only for strongly ST fluids, especially in large fractures. A Newtonian fluid tends to spread more across the open portion of the fracture plane, as compared to a ST fluid. Conversely, the ST behavior induces a more marked flow localization, with the flow presenting more extreme values of velocities under the same flow conditions.

The PDF of the velocity magnitude (i.e., the norm of the Eulerian velocity) is related to a typical transport attribute, the spatial-Lagrangian PDF, through flux-weighting (Dentz et al., 2016). Several studies have aimed at relating the Eulerian velocity PDF to porous medium's geometrical properties (de Anna et al., 2017; Hakoun et al., 2019; Puyguiraud et al., 2019a; Velásquez-Parra et al., 2021), and from there, anomalous transport to the Eulerian velocity PDF (Puyguiraud et al., 2019b; Velásquez-Parra et al., 2021). In Figure 8, the dimensionless PDF of velocity magnitudes is depicted to show the influence of rheology and fracture heterogeneity on the distribution of both high and low velocities. The dimensionless PDFs for the less ST fluid ($n = 0.61$) overlap with those for the Newtonian fluid for all the considered configurations, meaning that the fluid rheology does not affect the shape of the PDF but only its magnitude. Conversely, the more ST fluid ($n = 0.36$) shows more extreme values of the velocity magnitude under high pressure gradients, which corresponds physically to a higher localization of flow under a ST rheology than under the Newtonian rheology, as discussed above. The differences between the two non-Newtonian fluids for intermediate and high pressure gradients increase when a small fracture (i.e., $L/L_c = 1$) is considered, which is expected, since flow channeling at the fracture scale is much stronger in that case, even for Newtonian flow.

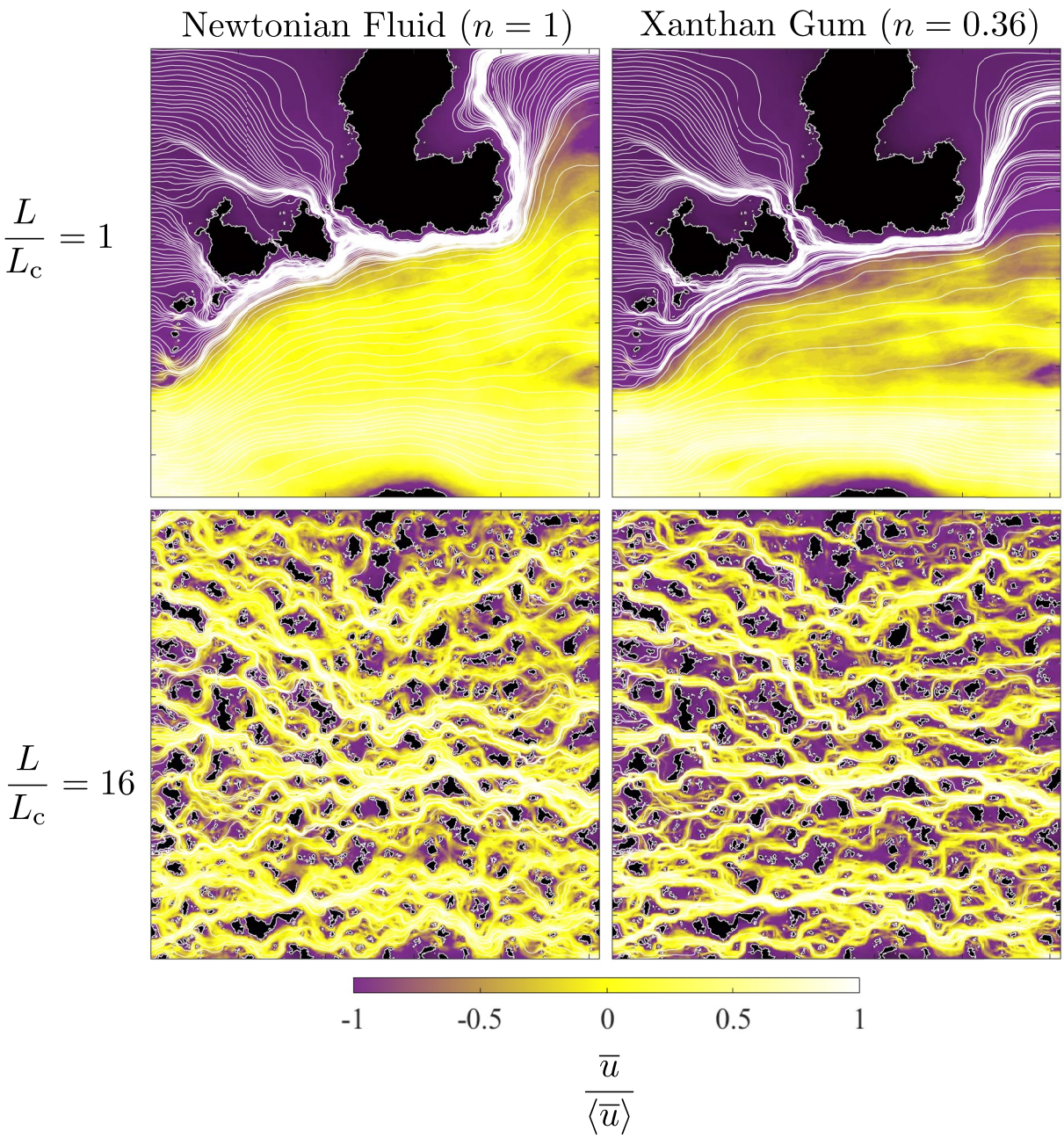


Figure 5. Spatial distribution, in the fracture plane, of the dimensionless velocity $\left(\overline{u}/\langle \overline{u} \rangle\right)$, for two fracture realizations with $L/L_c = 1$ (upper row) and $L/L_c = 16$ (lower row), respectively. The other geometrical parameters are $H = 0.8$, $\sigma_w/\langle w \rangle = 0.8$, $L_c = 0.1$ m, and $\langle w \rangle = 10^{-3}$ m for both realizations. Subfigures in the left hand column were obtained with a Newtonian rheology ($n = 1$), while those in the right-hand column depict the behavior of the xanthan gum solution (see Table 1), exhibiting stronger flow localization than the Newtonian flow.

4.2. Autocorrelation Function of the Velocity Components

In Figure 9, the autocorrelation functions of the velocity components are depicted for the case $L/L_c = 1$. The autocorrelation coefficients $\rho_{xx} = \text{Cov}\left(\overline{u}_x, \overline{u}_x\right)/\sigma^2_{\overline{u}_x}$ and $\rho_{yy} = \text{Cov}\left(\overline{u}_y, \overline{u}_y\right)/\sigma^2_{\overline{u}_y}$ are evaluated along their respective directions, that is, the x-direction and y-direction respectively. These autocorrelation functions provide a metric of disorder (Rozenbaum & Du Roscoat, 2014), which can be influenced by the fluid's rheology. These functions show a more rapid decay for strongly non-Newtonian fluids under high pressure gradient and in small fractures ($L/L_c = 1$), while larger fractures are not affected at all. All plots show a hole type covariance with zero

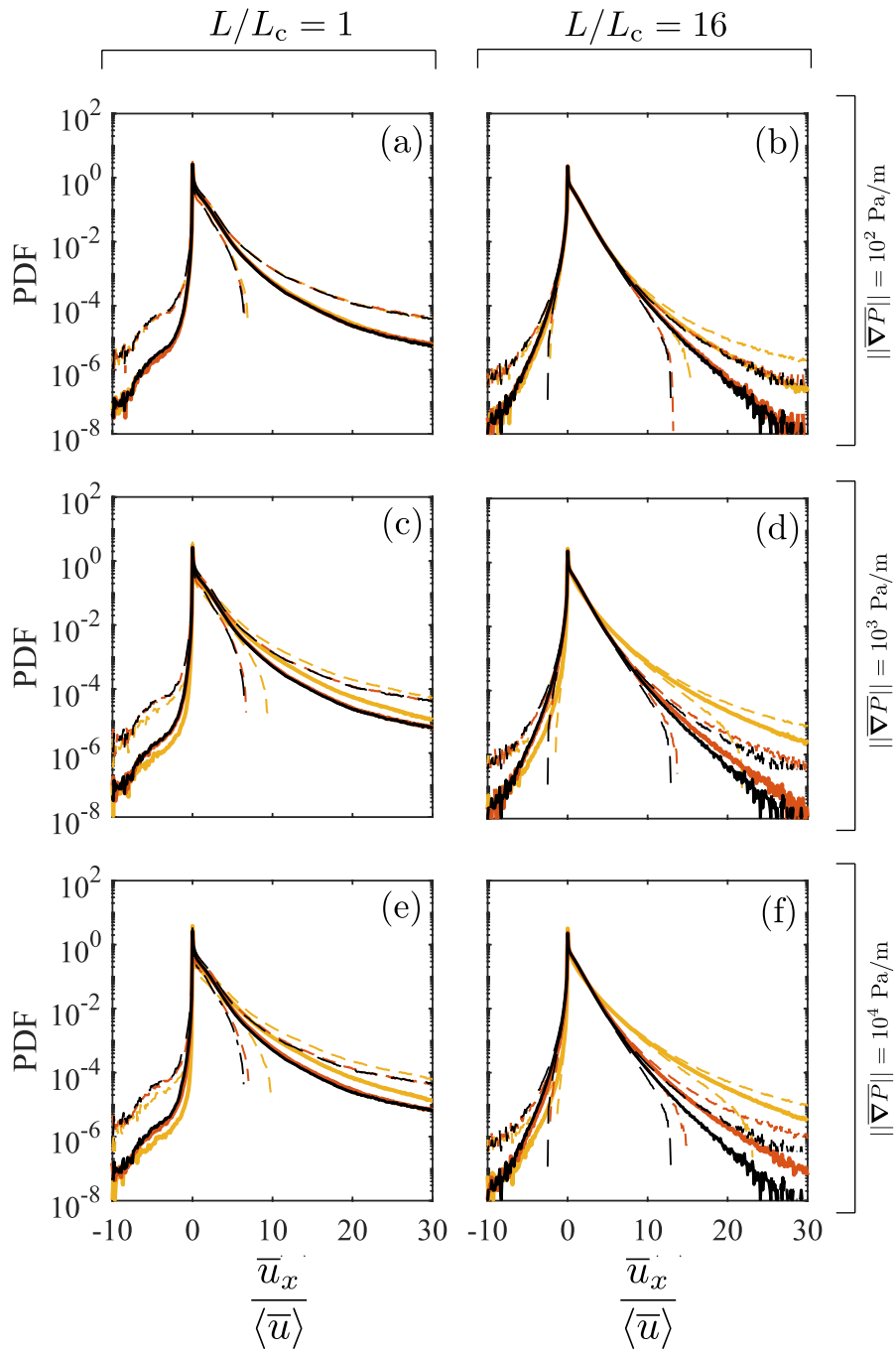


Figure 6. Probability density functions of the dimensionless longitudinal velocity component $\overline{u}_x/\langle \overline{u} \rangle$ for small (left column) and large (right column) fractures, and for small (top row), intermediate (middle row) and high (bottom row) macroscopic pressure gradients $\overline{\nabla P}$; solid lines represent the mean ensemble PDFs, while dashed lines define the confidence interval, with the range estimated considering the standard deviation. Black lines refer to the Newtonian case ($n = 1$), orange and yellow lines to the silicon oil ($n = 0.61$) and xanthan gum ($n = 0.36$), respectively.

integral scale: velocity fluctuations are positively correlated at short distances and negatively correlated at longer distances, and tend to zero exponentially from below. A similar structure has been obtained by Bellin et al. (1992) for 2-D porous media. The influence of rheology and of the external pressure gradient on the autocorrelation coefficients is almost imperceptible in the flow direction, while the transverse component is to some extent affected, showing a faster short-scale correlation decay as the fluid becomes more ST.

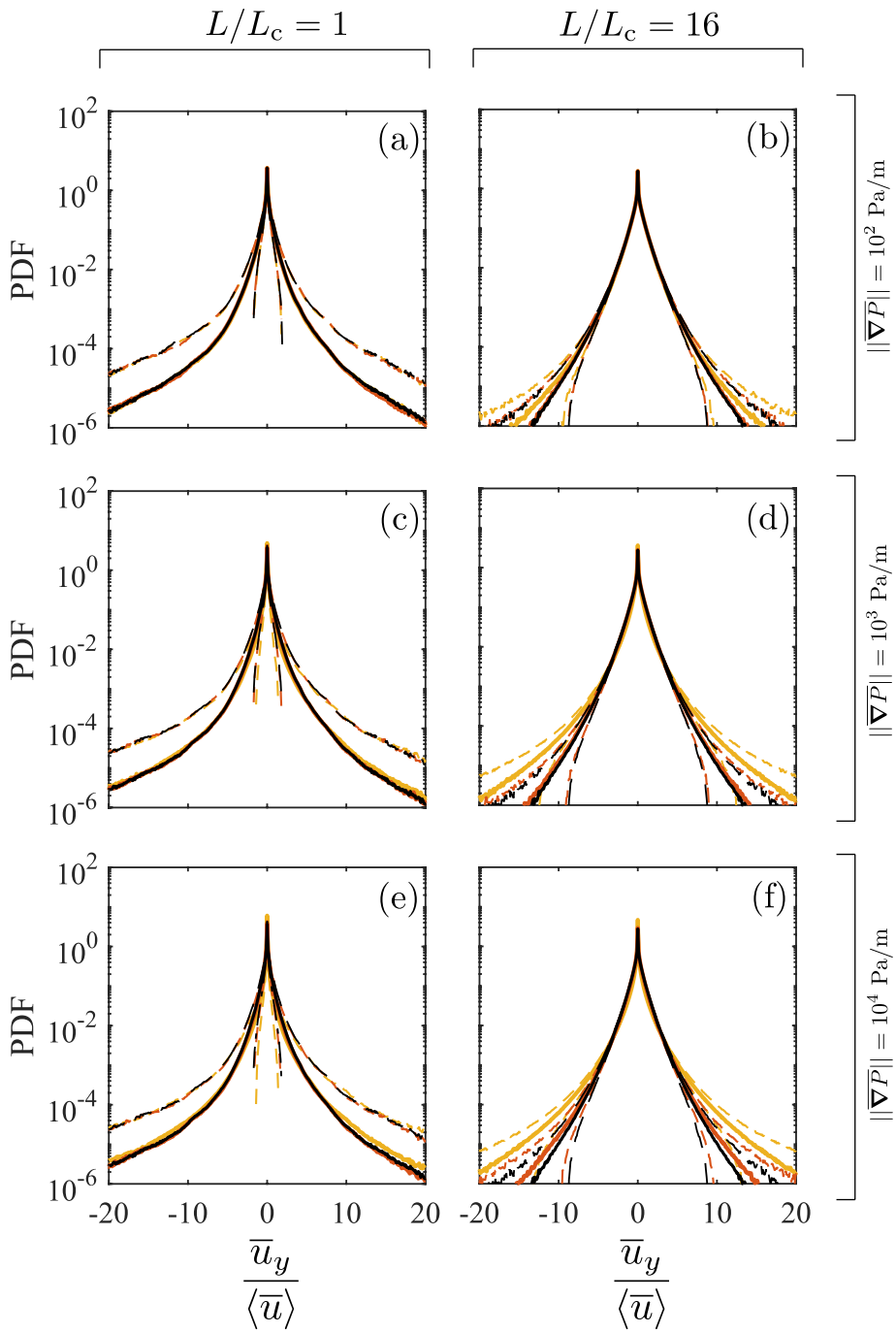


Figure 7. Probability density functions of the dimensionless transversal velocity component $u_y/\langle\overline{u}\rangle$ for small (left column) and large (right column) fractures, and for small (top row), intermediate (middle row) and high (bottom row) pressure gradients $\overline{\nabla P}$; solid lines represent the mean ensemble PDFs, while dashed lines define the confidence interval, with the range estimated considering the standard deviation. Black lines refer to the Newtonian case ($n = 1$), orange and yellow lines to the silicon oil ($n = 0.61$) and xanthan gum ($n = 0.36$), respectively.

Figure 10 depicts the autocorrelation coefficients for the case $L/L_c = 16$. All combinations of parameters result in the same hole covariances behavior for ρ_{xx} and ρ_{yy}: a narrow short-scale positive correlation, with a fast short-scale exponential decay, and a long-scale negative correlation, slowly tending to zero from below.

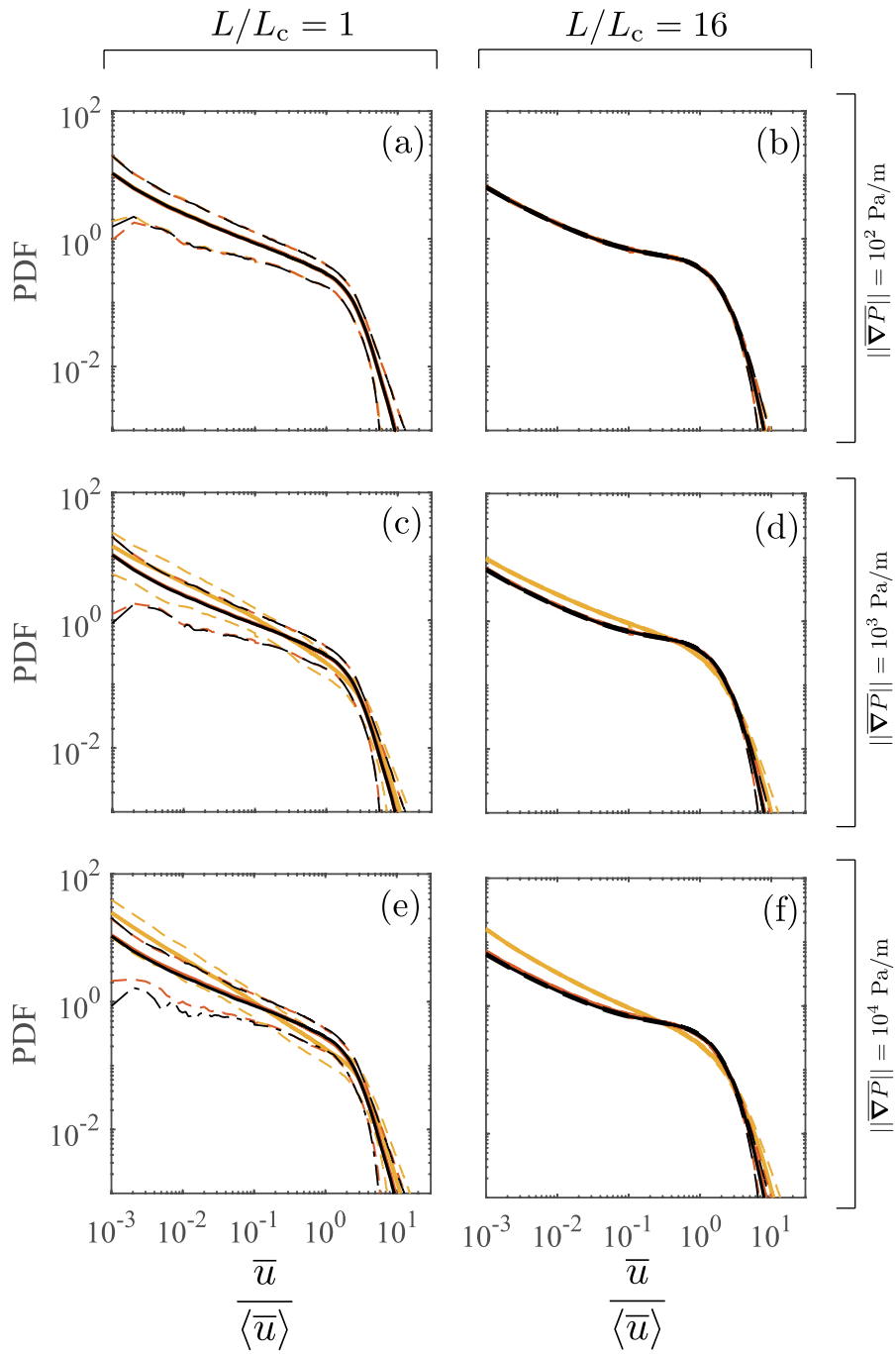


Figure 8. Probability density functions of the dimensionless velocity magnitude $\overline{u}/\langle\overline{u}\rangle$; for small (left column) and large (right column) fractures, and for small (top row), intermediate (middle row) and high (bottom row) pressure gradients $\overline{\nabla P}$; solid lines represent the mean ensemble PDFs, while dashed lines define the confidence interval, with the range estimated considering the standard deviation. Black lines refer to the Newtonian case ($n = 1$), orange and yellow lines to the silicon oil ($n = 0.61$) and xanthan gum ($n = 0.36$), respectively.

4.3. Fracture-Scale Hydraulic Behavior

Considering now the integral flow behavior, that is, the hydraulic behavior at the fracture scale, we see that the ST rheology enhances the fracture's apparent transmissivity: this effect becomes relevant under the action of a sufficiently large macroscopic pressure gradient (i.e., sufficiently large average velocity). Figure 11 depicts the dependence of the apparent transmissivity T, normalized with its Newtonian counterpart T_0, on the velocity

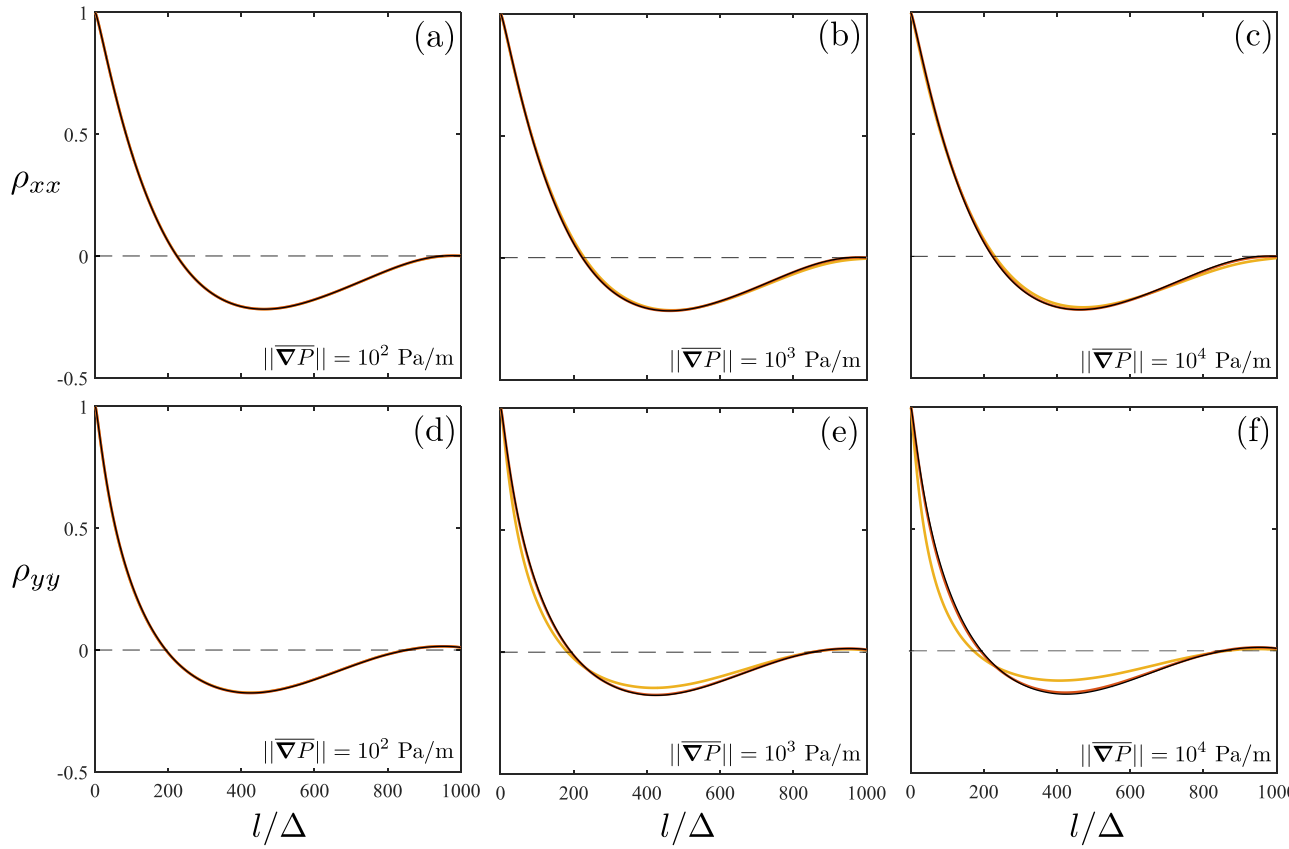


Figure 9. Autocorrelation functions, averaged over the MC simulations, of the velocity components (longitudinal ρ_{xx} and transversal ρ_{yy}) as a function of the dimensionless lag (l/Δ), for $L/L_c = 1$. The dimensionless lag is the ratio of the distance l to the mesh size Δ. Black lines refer to the Newtonian case ($n = 1$), orange and yellow lines to the silicon oil ($n = 0.61$) and xanthan gum ($n = 0.36$), respectively. The orange and the black lines overlap perfectly.

normalized by the characteristic flux q_c, for each realization; the average value for each Monte Carlo simulation is also shown. When the normalized velocity is smaller than 1, T/T_0 goes to 1, which is characteristic of the Darcian regime. When T/T_0 is sufficiently larger than 1, it is related to the normalized velocity through a non-linear relation in the form $\langle ||\mathbf{q}|| \rangle^n \propto || \nabla \langle P \rangle ||$, characteristic of the ST (power law) behavior. A similar macroscale transition between two such regimes has been observed for 2-D porous media by Zami-Pierre et al. (2016). Apparent transmissivity values obtained for small fractures ($L/L_c = 1$) are more disperse around their ensemble average as compared to their larger counterpart ($L/L_c = 16$), for which values for an individual realization are almost superimposed with their ensemble average. In other words, since no spatial correlations exist in the aperture field at scales larger than $L/16$, that field is mostly random and all realizations of it behave in the same way (see Méheust and Schmittbuhl (2003) for a similar result for Newtonian flow). However, comparing results for the two fractures shows that ensemble averages are almost insensitive to the fracture size, or, equivalently, to the ratio L/L_c. that is, the fluid's rheology dominates by far over aperture heterogeneities in controlling the hydraulic behavior for such strongly ST fluids.

5. Conclusions

We conducted a comprehensive stochastic analysis aimed at elucidating how the effects of ST rheology and aperture variability impact the flow in realistic synthetic geological fractures. Our results provide an insight on the interplay between the fluid's ST nature and the fracture's heterogeneity, covering the entire range of variability of the fluid ST index, fracture size to correlation length ratio, and imposed macroscopic pressure gradient. The ST behavior of the fluid, modeled by means of the three-parameter Ellis rheology, is particularly relevant when the fracture is subjected to a sufficiently high macroscopic pressure gradient (typical of forced regimes). A transition from the Darcian regime $\langle ||\mathbf{q}|| \rangle \propto ||\nabla P||$ to the non-linear regime $\langle ||\mathbf{q}|| \rangle^n \propto ||\nabla P||$ occurs when increasing

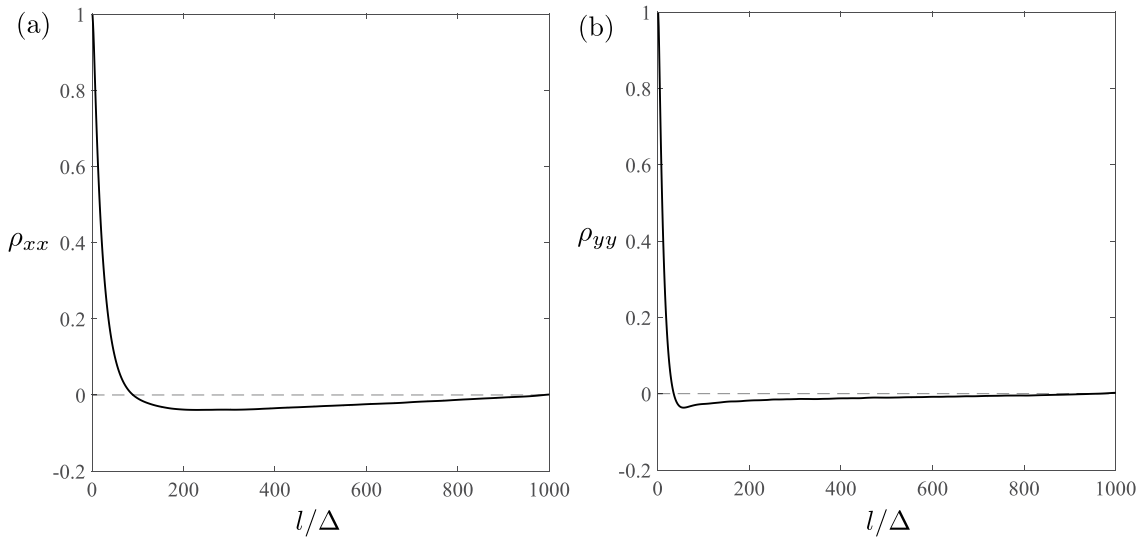


Figure 10. Autocorrelation functions, averaged over the MC simulations, of the velocity components (longitudinal ρ_{xx} and transversal ρ_{yy}) as a function of the dimensionless lag (l/Δ), for $L/L_c = 16$. The dimensionless lag is the ratio of the distance l to the mesh size Δ. The lines corresponding to the different fluids overlap perfectly with the black solid line.

the imposed macroscopic pressure gradient. Under the same conditions, the ensemble statistics of the velocity components differ more from the Newtonian case for a more ST fluid. In particular, the average PDFs of the normalized velocity components show thicker tails for ST rheologies, indicating a higher frequency of velocities much larger than the mean value. The average PDFs of the velocity magnitude also display a higher dispersion of the velocity around the mean values. These results can be explained by the fact that for more strongly ST fluids the flow localization on correlated large aperture channels is more intense. This stronger flow localization is consistent with results obtained on 2-D porous media in earlier studies. In rough fractures, however, long range spatial correlations create channeling at the scale of the correlation length, which is then the longitudinal scale at which flow localization occurs; this is an ingredient that is not present in uncorrelated 2-D porous media.

In sum, the flow pattern is mostly governed by aperture heterogeneities, while the impact of the fluid rheology on the probability density function of velocity components, once normalized by the mean velocity, is relatively limited, except for ST fluids with a very low power law index. The fracture scale hydraulic behavior, on the other hand, is strongly affected by the fluid rheology: the ratio of apparent non-Newtonian transmissivities to those

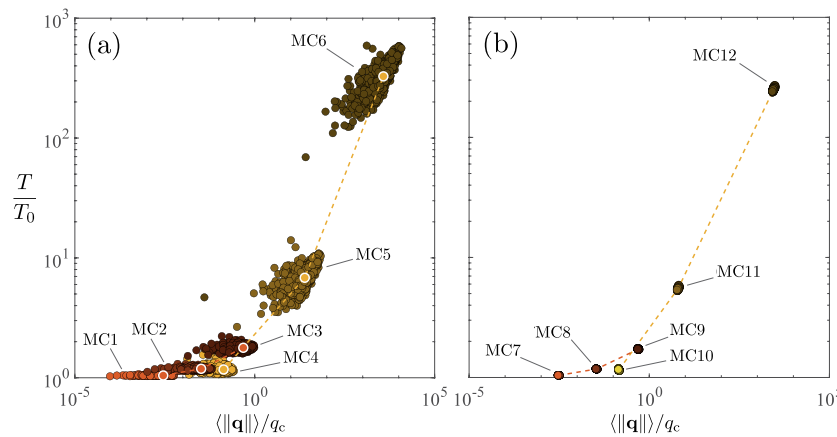


Figure 11. Dependence of the dimensionless transmissivity T/T_0 on the dimensionless local flux, $\langle \|\mathbf{q}\| \rangle / q_c$, for all realizations and the ensemble average of each Monte Carlo simulation: (a) $L/L_c = 1$, (b) $L/L_c = 16$. Simulation results for the silicon oil and xanthan gum are in orange and yellow, respectively; the darker the color, the higher the imposed global pressure gradient is. Lines are a guide to the eyes.

obtained for Newtonian flow increases with the ST power law index, reaching values much larger than unity. Ensemble averages of the overall hydraulic transmissivity are almost independent of the fracture size (or, equivalently, of the ratio L/L_c), but smaller fractures (i.e., those with larger L/L_c ratios), whose transmissivities are more affected by structural disorder due to flow channeling up to the fracture scale (as for Newtonian flow), show a larger apparent dispersion around the mean apparent transmissivity. Though the study was performed here on two given ST fluids, the generalization of our results to any ST fluid is straightforward: the increase in the fracture's hydraulic behavior under ST flow, as compared to the Newtonian behavior, is controlled by the fluid's power law index n, and is observed for applied macroscopic pressure gradients larger than a critical value; that critical value can be predicted from the rheology (Equations 14 and (15)). Equivalently, global ST flow behavior occurs if the mean local flux is larger than a critical value whose analytical expression is given by Equation 16.

The analysis of the velocity statistics proposed in this work will be used in a similar Monte Carlo framework to characterize solute transport (e.g., through spatial dispersion or breakthrough curves).

Data Availability Statement

There are no data sharing issues since all of the numerical information is provided in the figures produced by solving the equations in the paper.

Acknowledgments
A. Lenci, Y. Méheust and V. Di Federico acknowledge support from the University of Bologna through the following programs, respectively: the Marco Polo Grant 2019, Visiting Professor Fellowship Excellence Department Project 2020, and ALMAIDEA Grant 2017. Open Access Funding provided by University of Bologna.

References

Ansari, M., Turney, D. E., Morris, J., & Banerjee, S. (2021). Investigations of rheology and a link to microstructure of oil-based drilling fluids. *Journal of Petroleum Science and Engineering*, *196*, 108031. https://doi.org/10.1016/j.petrol.2020.108031

Auradou, H., Boschan, A., Chertcoff, R., Gabbanelli, S., Hulin, J., & Ippolito, I. (2008). Enhancement of velocity contrasts by shear-thinning solutions flowing in a rough fracture. *Journal of Non-Newtonian Fluid Mechanics*, *153*(1), 53–61. https://doi.org/10.1016/j.jnnfm.2007.11.008

Bächler, D., Kohl, T., & Rybach, L. (2003). Impact of graben-parallel faults on hydrothermal convection—Rhine graben case study. *Physics and Chemistry of the Earth, Parts A/B/C*, *28*(9–11), 431–441. https://doi.org/10.1016/s1474-7065(03)00063-9

Barati, R., & Liang, J.-T. (2014). A review of fracturing fluid systems used for hydraulic fracturing of oil and gas wells. *Journal of Applied Polymer Science*, *131*(16). https://doi.org/10.1002/app.40735

Barbati, A. C., Desroches, J., Robisson, A., & McKinley, G. H. (2016). Complex fluids and hydraulic fracturing. *Annual Review of Chemical and Biomolecular Engineering*, *7*(1), 415–453. https://doi.org/10.1146/annurev-chembioeng-080615-033630

Bellin, A., Salandin, P., & Rinaldo, A. (1992). Simulation of dispersion in heterogeneous porous formations: Statistics, first-order theories, convergence of computations. *Water Resources Research*, *28*(9), 2211–2227. https://doi.org/10.1029/92wr00578

Berkowitz, B. (1994). *Advances in porous media*. In M. Corapcioglu (Ed.), (pp. 397–451). : Elsevier.

Berkowitz, B., & Scher, H. (1998). Theory of anomalous chemical transport in random fracture networks. *Physical Review E - Statistical Physics, Plasmas, Fluids, and Related Interdisciplinary Topics*, *57*(5), 5858–5869. https://doi.org/10.1103/physreve.57.5858

Boffa, J., Allain, C., Chertcoff, R., Hulin, J., Plouraboué, F., & Roux, S. (1999). Roughness of sandstone fracture surfaces: Profilometry and shadow length investigations. *European Physical Journal B*, *7*(2), 179–182. https://doi.org/10.1007/s100510050602

Bouchaud, E. (1997). Scaling properties of cracks. *Journal of Physics: Condensed Matter*, *9*(21), 4319–4344. https://doi.org/10.1088/0953-8984/9/21/002

Bouchaud, E., Lapasset, G., & Planès, J. (1990). Fractal dimension of fractured surfaces: A universal value? *Europhysics Letters*, *13*(1), 73–79. https://doi.org/10.1209/0295-5075/13/1/013

Brown, S. R. (1987). Fluid flow through rock joints: The effect of surface roughness. *Journal of Geophysical Research*, *92*(B2), 1337. https://doi.org/10.1029/jb092ib02p01337

Brown, S. R. (1995). Simple mathematical model of a rough fracture. *Journal of Geophysical Research*, *100*(B4), 5941–5952. https://doi.org/10.1029/94jb03262

Brown, S. R., & Scholz, C. H. (1985). Broad bandwidth study of the topography of natural rock surfaces. *Geophysical Research*.

Candela, T., Renard, F., Bouchon, M., Brouste, A., Marsan, D., Schmittbuhl, J., & Voisin, C. (2009). Characterization of fault roughness at various scales: Implications of three-dimensional high resolution topography measurements. *Pure and Applied Geophysics*, *166*(10–11), 1817–1851. https://doi.org/10.1007/s00024-009-0521-2

Carreau, P. J. (1972). Rheological equations from molecular network theories. *Transactions of the Society of Rheology*, *16*(1), 99–127. https://doi.org/10.1122/1.549276

Chiapponi, L., Ciriello, V., Longo, S., & Federico, V. D. (2019). Non-Newtonian backflow in an elastic fracture. *Water Resources Research*, *55*(12), 10144–10158. https://doi.org/10.1029/2019wr026071

Cipolla, C. L., Warpinski, N. R., Mayerhofer, M. J., Lolon, E., & Vincent, M. C. (2008). The relationship between fracture complexity, reservoir properties, and fracture treatment design. *All Days SPE*. https://doi.org/10.2118/115769-ms

Ciriello, V., Lenci, A., Longo, S., & Federico, V. D. (2021). Relaxation-induced flow in a smooth fracture for Ellis rheology. *Advances in Water Research*, *152*, 103914. https://doi.org/10.1016/j.advwatres.2021.103914

Comolli, A., Hakoun, V., & Dentz, M. (2019). Mechanisms, upscaling, and prediction of anomalous dispersion in heterogeneous porous media. *Water Resources Research*, *55*(10), 8197–8222. https://doi.org/10.1029/2019wr024919

Cox, B., & Wang, J. S. Y. (1993). Fractal surfaces:measurement and application in Earth sciences. *Fractals*, *01*(01), 87–115. https://doi.org/10.1142/s0218348x93000125

De Anna, P., Quaife, B., Biros, G., & Juanes, R. (2017). Prediction of the low-velocity distribution from the pore structure in simple porous media. *Physical Review Fluids*, *2*(12), 124103.

De Dreuzy, J.-R., Méheust, Y., & Pichot, G. (2012). Influence of fracture scale heterogeneity on the flow properties of three-dimensional discrete fracture networks (DFN). *Journal of Geophysical Research*, *117*, B11207. https://doi.org/10.1029/2012JB009461

Dejam, M. (2019). Advective-diffusive-reactive solute transport due to non-Newtonian fluid flows in a fracture surrounded by a tight porous medium. *International Journal of Heat andMass Transfer*, *128*, 1307–1321. https://doi.org/10.1016/j.ijheatmasstransfer.2018.09.061

Dentz, M., Kang, P. K., Comolli, A., Borgne, T. L., & Lester, D. R. (2016). Continuous time random walks for the evolution of Lagrangian velocities. *Physical Review Fluids*, *1*(7), 074004. https://doi.org/10.1103/physrevfluids.1.074004

Di Federico, V. (1997). Estimates of equivalent aperture for non-Newtonian flow in a rough-walled fracture. *International Journal of Rock Mechanics and Mining Sciences*, *34*(7), 1133–1137. https://doi.org/10.1016/s1365-1609(97)90205-7

Elsworth, D., & Goodman, R. (1986). Characterization of rock fissure hydraulic conductivity using idealized wall roughness profiles. *International Journal of Rock Mechanics and Mining Sciences & Geomechanics Abstracts*, *23*(3), 233–243. https://doi.org/10.1016/0148-9062(86)90969-1

Felisa, G., Lenci, A., Lauriola, I., Longo, S., & Di Federico, V. (2018). Flow of truncated power-law fluid in fracture channels of variable aperture. *Advances in Water Resources*, *122*, 317–327. https://doi.org/10.1016/j.advwatres.2018.10.024

Feng, Y., & Gray, K. (2017). Review of fundamental studies on lost circulation and wellbore strengthening. *Journal of Petroleum Science and Engineering*, *152*, 511–522. https://doi.org/10.1016/j.petrol.2017.01.052

Fournier, A., Fussell, D., & Carpenter, L. (1982). Computer rendering of stochastic models. *Communications of the ACM*, *25*(6), 371–384. https://doi.org/10.1145/358523.358553

Gale, J. (1990). *Rock joints*. In N. Barton & O. Stephansson (Eds.), (pp. 351–362).

Gómez-Hernández, J., & Wen, X.-H. (1998). To be or not to be multi-Gaussian? A reflection on stochastic hydrogeology. *Advances in Water Resources*, *21*(1), 47–61. https://doi.org/10.1016/s0309-1708(96)00031-0

Gutfraind, R., Ippolito, I., & Hansen, A. (1995). Study of tracer dispersion in self-affine fractures using lattice–gas automata. *Physics of Fluids*, *7*(8), 1938–1948. https://doi.org/10.1063/1.868508

Hakoun, V., Comolli, A., & Dentz, M. (2019). Upscaling and prediction of Lagrangian velocity dynamics in heterogeneous porous media. *Water Resources Research*, *55*(5), 3976–3996. https://doi.org/10.1029/2018wr023810

Hayek, M., RamaRao, B. S., & Lavenue, M. (2020). An adjoint sensitivity model for transient sequentially coupled radionuclide transport in porous media. *Water Resources Research*, *56*(7), e2020WR027274. https://doi.org/10.1029/2020wr027274

Hirasaki, G. J., Miller, C. A., & Puerto, M. (2011). Recent advances in surfactant EOR. *SPE Journal*, *16*(04), 889–907. https://doi.org/10.2118/115386-pa

Jung, R. (1989). Hydraulic in situ investigations of an artificial fracture in the Falkenberg granite. *International Journal of Rock Mechanics and Mining Sciences & Geomechanics Abstracts*, *26*(3–4), 301–308. https://doi.org/10.1016/0148-9062(89)91978-5

Katiyar, A., Agrawal, S., Ouchi, H., Seleson, P., Foster, J. T., & Sharma, M. M. (2020). A general peridynamics model for multiphase transport of non-Newtonian compressible fluids in porous media. *Journal of Computational Physics*, *402*, 109075. https://doi.org/10.1016/j.jcp.2019.109075

Koranne, S. (2010). Hierarchical data format 5: HDF5. In *Handbook of open source tools* (pp. 191–200). Springer US. https://doi.org/10.1007/978-1-4419-7719-9_10

Larson, R. G. (1992). Instabilities in viscoelastic flows. *Rheologica Acta*, *31*(3), 213–263. https://doi.org/10.1007/bf00366504

Lavrov, A. (2013). Numerical modeling of steady-state flow of a non-Newtonian power-law fluid in a rough-walled fracture. *Computers and Geotechnics*, *50*, 101–109. https://doi.org/10.1016/j.compgeo.2013.01.004

Lenci, A., & Di Federico, V. (2020). A channel model for bi-viscous fluid flow in fractures. *Transport in Porous Media*, *134*(1), 97–116. https://doi.org/10.1007/s11242-020-01438-5

Lenci, A., Putti, M., Federico, V. D., & Méheust, Y. (2022). A lubrication-based solver for shear-thinning flow in rough fractures. *Water Resources Research*, *58*(8), e2021WR031760. https://doi.org/10.1029/2021wr031760

Leung, D. Y., Caramanna, G., & Maroto-Valer, M. M. (2014). An overview of current status of carbon dioxide capture and storage technologies. *Renewable Sustainable Energy Reviews*, *39*, 426–443. https://doi.org/10.1016/j.rser.2014.07.093

Lu, S., Molz, F. J., & Liu, H. H. (2003). An efficient, three-dimensional, anisotropic, fractional Brownian motion and truncated fractional levy motion simulation algorithm based on successive random additions. *Computers and Geotechnics*, *29*(1), 15–25. https://doi.org/10.1016/S0098-3004(02)00073-0

Magzoub, M., Salehi, S., Li, G., Fan, J., & Teodoriu, C. (2021). Loss circulation prevention in geothermal drilling by shape memory polymer. *Geothermics*, *89*, 101943. https://doi.org/10.1016/j.geothermics.2020.101943

Makurat, A. (1985). The effect of shear displacement on the permeability of natural rough joints. In S. Neuman & E. Simpson (Eds.), *Proceedings of the memoirs of hte 17th int. congress of IAH* (pp. 99–106).

Matsumoto, M., & Nishimura, T. (1998). Mersenne twister. *ACM Transactions on Modeling and Computer Simulation*, *8*(1), 3–30. https://doi.org/10.1145/272991.272995

Meakin, P., & Tartakovsky, A. M. (2009). Modeling and simulation of pore-scale multiphase fluid flow and reactive transport in fractured and porous media. *Reviews of Geophysics*, *47*(3), RG3002. https://doi.org/10.1029/2008rg000263

Méheust, Y., Parmar, K. P. S., Schjelderupsen, B., & Fossum, J. O. (2011). The electrorheology of suspensions consisting of Na-fluorohectorite synthetic clay particles in silicon oil. *Journal of Rheology*, *55*(4), 809–833.

Méheust, Y., & Schmittbuhl, J. (2000). Flow enhancement of a rough fracture. *Geophysical Research Letters*, *27*(18), 2989–2992. https://doi.org/10.1029/1999gl008464

Méheust, Y., & Schmittbuhl, J. (2001). Geometrical heterogeneities and permeability anisotropy of rough fractures. *Journal of Geophysical Research*, *106*(B2), 2089–2102. https://doi.org/10.1029/2000jb900306

Méheust, Y., & Schmittbuhl, J. (2003). Scale effects related to flow in rough fractures. *Pure and Applied Geophysics*, *160*(5), 1023–1050. https://doi.org/10.1007/pl00012559

Moreno, L., Tsang, Y. W., Tsang, C. F., Hale, F. V., & Neretnieks, I. (1988). Flow and tracer transport in a single fracture: A stochastic model and its relation to some field observations. *Water Resources Research*, *24*(12), 2033–2048. https://doi.org/10.1029/wr024i012p02033

Morris, J. P., Chochua, G. G., & Bogdan, A. V. (2015). An efficient non-Newtonian fluid-flow simulator for variable aperture fractures. *Canadian Journal of Chemical Engineering*, *93*(11), 1902–1915. https://doi.org/10.1002/cjce.22314

Moukhtari, F.-E., & Lecampion, B. (2018). A semi-infinite hydraulic fracture driven by a shear-thinning fluid. *Journal of Fluid Mechanics*, *838*, 573–605. https://doi.org/10.1017/jfm.2017.900

Mourzenko, V. V., Thovert, J.-F., & Adler, P. M. (1995). Permeability of a single fracture: Validity of the Reynolds equation. *Journal de Physique: II*, *5*(3), 465–482. https://doi.org/10.1051/jp2:1995133

Neuzil, C. E., & Tracy, J. V. (1981). Flow through fractures. *Water Resources Research*, *17*(1), 191–199. https://doi.org/10.1029/wr017i001p00191

Nigon, B., Englert, A., Pascal, C., & Saintot, A. (2017). Multiscale characterization of joint surface roughness. *Journal of Geophysical Research: Solid Earth*, *122*(12), 9714–9728. https://doi.org/10.1002/2017jb014322

Nowamooz, A., Radilla, G., Fourar, M., & Berkowitz, B. (2013). Non-fickian transport in transparent replicas of rough-walled rock fractures. *Transport in Porous Media*, *98*(3), 651–682. https://doi.org/10.1007/s11242-013-0165-7

Pahari, S., Bhandakkar, P., Akbulut, M., & Kwon, J. S.-I. (2021). Optimal pumping schedule with high-viscosity gel for uniform distribution of proppant in unconventional reservoirs. *Energy*, *216*, 119231. https://doi.org/10.1016/j.energy.2020.119231

Parmar, K. P. S., Méheust, Y., & Fossum, J. O. (2008). Electrorheological suspensions of laponite in oil: Rheometry studies. *Langmuir*, *24*, 1814–1822. https://doi.org/10.1021/la702989u

Perkowska, M., Wrobel, M., & Mishuris, G. (2016). Universal hydrofracturing algorithm for shear-thinning fluids: Particle velocity based simulation. *Computers and Geotechnics*, *71*, 310–337. https://doi.org/10.1016/j.compgeo.2015.10.005

Plouraboué, F., Hulin, J.-P., Roux, S., & Koplik, J. (1998). Numerical study of geometrical dispersion in self-affine rough fractures. *Physical Review E - Statistical Physics, Plasmas, Fluids, and Related Interdisciplinary Topics*, *58*(3), 3334–3346. https://doi.org/10.1103/physreve.58.3334

Puyguiraud, A., Gouze, P., & Dentz, M. (2019a). Stochastic dynamics of Lagrangian pore-scale velocities in three-dimensional porous media. *Water Resources Research*, *55*(2), 1196–1217. https://doi.org/10.1029/2018wr023702

Puyguiraud, A., Gouze, P., & Dentz, M. (2019b). Upscaling of anomalous pore-scale dispersion. *Transport in Porous Media*, *128*(2), 837–855. https://doi.org/10.1007/s11242-019-01273-3

Rozenbaum, O., & Du Roscoat, S. R. (2014). Representative elementary volume assessment of three-dimensional x-ray microtomography images of heterogeneous materials: Application to limestones. *Physical Review E - Statistical Physics, Plasmas, Fluids, and Related Interdisciplinary Topics*, *89*(5), 053304. https://doi.org/10.1103/physreve.89.053304

Schmittbuhl, J., Gentier, S., & Roux, S. (1993). Field measurements of the roughness of fault surfaces. *Geophysical Research Letters*, *20*(8), 639–641. https://doi.org/10.1029/93gl00170

Schmittbuhl, J., Schmitt, F., & Scholz, C. (1995). Scaling invariance of crack surfaces. *Journal of Geophysical Research*, *100*(B4), 5953–5973. https://doi.org/10.1029/94jb02885

Schmittbuhl, J., Vilotte, J.-P., & Roux, S. (1995). Reliability of self-affine measurements. *Physical Review E - Statistical Physics, Plasmas, Fluids, and Related Interdisciplinary Topics*, *51*(1), 131–147. https://doi.org/10.1103/physreve.51.131

Siena, M., Riva, M., Hyman, J. D., Winter, C. L., & Guadagnini, A. (2014). Relationship between pore size and velocity probability distributions in stochastically generated porous media. *Physical Review E - Statistical Physics, Plasmas, Fluids, and Related Interdisciplinary Topics*, *89*(1), 013018. https://doi.org/10.1103/physreve.89.013018

Starchenko, V., Marra, C. J., & Ladd, A. J. C. (2016). Three-dimensional simulations of fracture dissolution. *Journal of Geophysical Research: Solid Earth*, *121*(9), 6421–6444. https://doi.org/10.1002/2016jb013321

Stockman, H. W. (1997). A lattice gas study of retardation and dispersion in fractures: Assessment of errors from desorption kinetics and buoyancy. *Water Resources Research*, *33*(8), 1823–1831. https://doi.org/10.1029/97wr01228

Tian, Z., & Wang, J. (2017). Lattice Boltzmann simulation of CO2 reactive transport in network fractured media. *Water Resources Research*, *53*(8), 7366–7381. https://doi.org/10.1002/2017wr021063

Tsang, Y. W., & Tsang, C. F. (1987). Channel model of flow through fractured media. *Water Resources Research*, *23*(3), 467–479. https://doi.org/10.1029/wr023i003p00467

Uddin, J., Marston, J. O., & Thoroddsen, S. T. (2012). Squeeze flow of a Carreau fluid during sphere impact. *Physics of Fluids*, *24*(7), 073104. https://doi.org/10.1063/1.4736742

Velásquez-Parra, A., Aquino, T., Willmann, M., Méheust, Y., Le Borgne, T., & Jiménez-Martínez, J. (2021). Sharp transition to strongly anomalous transport in unsaturated porous media. *Geophysical Research Letters*, e2021GL096280.

Wang, S., Tang, H., Guo, J., & Wang, K. (2016). Effect of pH on the rheological properties of borate crosslinked hydroxypropyl guar gum hydrogel and hydroxypropyl guar gum. *Carbohydrate Polymers*, *147*, 455–463. https://doi.org/10.1016/j.carbpol.2016.04.029

Wilson, C. R., & Witherspoon, P. A. (1974). Steady state flow in rigid networks of fractures. *Water Resources Research*, *10*(2), 328–335. https://doi.org/10.1029/wr010i002p00328

Wrobel, M., Mishuris, G., & Papanastasiou, P. (2021). On the influence of fluid rheology on hydraulic fracture. *International Journal of Engineering Science*, *158*, 103426. https://doi.org/10.1016/j.ijengsci.2020.103426

Yang, H. J., Boso, F., Tchelepi, H. A., & Tartakovsky, D. M. (2020). Method of distributions for quantification of geologic uncertainty in flow simulations. *Water Resources Research*, *56*(7), e2020WR027643. https://doi.org/10.1029/2020wr027643

Yeo, I., De Freitas, M., & Zimmerman, R. (1998). Effect of shear displacement on the aperture and permeability of a rock fracture. *International Journal of Rock Mechanics and Mining Sciences*, *35*(8), 1051–1070. https://doi.org/10.1016/s0148-9062(98)00165-x

Zami-Pierre, F., De Loubens, R., Quintard, M., & Davit, Y. (2016). Transition in the flow of power-law fluids through isotropic porous media. *Physical Review Letters*, *117*(7), 074502. https://doi.org/10.1103/physrevlett.117.074502

Zhong, Z., Sun, A. Y., & Jeong, H. (2019). Predicting CO 2 plume migration in heterogeneous formations using conditional deep convolutional generative adversarial network. *Water Resources Research*, *55*(7), 5830–5851. https://doi.org/10.1029/2018wr024592

Zimmerman, R. W., & Bodvarsson, G. S. (1996). Hydraulic conductivity of rock fractures. *Transport in Porous Media*, *23*(1). https://doi.org/10.1007/bf00145263